ACS APPLIED ENERGY MATERIALS

www.acsaem.org

Article

CO_2 is Converted into Renewable Energy and Green Products in a Membraneless Solar-Driven Fuel Cell

Luiz Eduardo Gomes,* Bárbara A.C. Sá, Márcio C. Pereira, Luiz Felipe Plaça, Maximiliano J. M. Zapata, Mohammed A. M. Bajiri, Niqab Khan, Glaucia B. Alcantara, André Luis de Jesus Pereira, Renato V. Gonçalves, Cauê A. Martins, and Heberton Wender*

Cite This: *ACS Appl. Energy Mater.* 2026, 9, 2197−2208

Read Online

ACCESS | Metrics & More | Article Recommendations | Supporting Information

ABSTRACT: The urgent need for innovative renewable energy technologies and strategies to reduce greenhouse gas emissions is increasingly critical for global sustainability. Photocatalytic fuel cells (PFCs) present a promising solution by integrating solar energy harvesting with the direct and spontaneous conversion of chemical energy into electricity, not only achieving zero carbon emissions but also generating carbon credits. In this study, we developed $BiVO_4$/WO_3/V_2O_5 photoanodes and Cu_2O/CuO photocathodes for a single-compartment, membraneless, solar-driven fuel cell that simultaneously converts CO_2 and sulfite ions into electrical power and green fuels. Our optimized device achieved an open-circuit voltage of 0.50 V, a short-circuit current of 0.50 mA cm^{-2}, and a maximum output power of 0.05 mW cm^{-2} at one sun illumination. We extensively characterized the photoelectrodes' morphology and their structural, optical, and electronic properties to elucidate the PFC's operating mechanism. The device primarily produced ethanol from CO_2 reduction, followed by formate, acetate, and methanol as liquid products. In the gas phase, CH_4 was the sole product from CO_2 conversion, with a Faradaic efficiency (FE) of 40.8% at zero voltage bias, and hydrogen evolution accounted for only 0.5% FE. Overall, our PFC device demonstrates the capability to spontaneously generate renewable electric power and green fuels at ambient pressure and temperature, using solar energy as the only driving force.

KEYWORDS: *photocatalytic fuel cell, CO_2 reduction, photoelectrochemical conversion, photoanode, photocathode, solar fuels*

1. INTRODUCTION

In recent decades, the growth of industrial activity and dependence on fossil fuels have led to increasing concentrations of greenhouse gases in the Earth's atmosphere, particularly carbon dioxide (CO_2). This has motivated the investigation of different approaches to mitigate CO_2, including thermochemical, electrochemical, and photochemical processes.[1−4] The electrochemical CO_2 reduction reaction (CO_2RR) is a promising approach for converting CO_2 into chemicals such as methanol, ethanol, methane, and formate using renewable energy sources, particularly solar energy.[5,6] It may enable the creation of a carbon-neutral cycle that reduces dependence on fossil fuels and decreases the environmental impact of CO_2 emissions.

Among the CO_2RR processes, photoelectrochemical (PEC) devices and photocatalytic fuel cells (PFCs) are particularly interesting since they can convert solar energy directly.[7−9] Figure 1 highlights the similarities and differences between these two systems. Solar fuel generators that contain a solid/electrolyte junction are referred to as PEC cells, and several subclassifications have been described.[10] In a PEC system, light excitation generates electron−hole pairs in a semiconductor electrode. However, external voltage is usually required to drive coupled oxidation and reduction reactions, as in the case of photoelectrolysis or CO_2 reduction. It can be performed with or without sacrificial agents such as methanol or SO_3^{2-}, among others, to decrease the external electrical input required and increase overall activity due to the slow kinetics of the water oxidation half-reaction. When the PEC cell only operates through a voltage bias-driven process, it is thermodynamically nonspontaneous ($\Delta G > 0$), where external electrical energy input is necessary to sustain the coupled redox reaction (Figure 1A). In contrast, a PFC operates spontaneously ($\Delta G < 0$),[7,8] where photoexcited charge carriers flow naturally due to the

Received: November 21, 2025
Revised: January 6, 2026
Accepted: January 19, 2026
Published: February 2, 2026

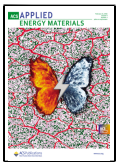

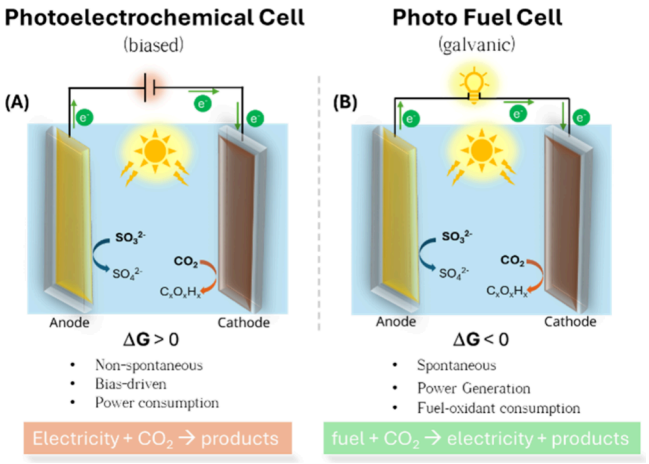

Figure 1. Schematic representation comparing (a) a PEC CO_2 reduction full cell under an applied bias and (b) a PFC fed by CO_2 (oxidant) and sulfite as fuel. Both diagrams depict systems without a separation membrane between the two photoelectrodes, as investigated in this work, with labeled arrows indicating reactants, products, and electron flow. However, the concept is also applicable to H-type cells with a separation membrane, as well as to systems with a single semiconductor-based electrode under light illumination.

intrinsic potential difference between two electrodes—at least one of which is light-active and under illumination—allowing simultaneous power generation without an external voltage bias (Figure 1B).[11,12] Unlike a biased-PEC system, which operates as an intrinsically solar-powered electrolyzer, a PFC is a hybrid device that combines photocatalysis and fuel cell principles to harness solar and chemical energy to simultaneously generate electricity and valuable products—in certain cases, green fuels—such as when CO_2 serves as the oxidant. Therefore, a PFC is a self-sustained solar energy converter, operating through a coupled redox reaction that generates power directly once we ensure the reduction reaction potential exceeds the oxidation one (detailed discussion in due course). As for a PEC electrolyzer, a PFC may be engineered using a single photoelectrode (a dark electrode combined with a photocathode or a photoanode) or a dual-photoelectrode configuration. The dual-photoelectrode configuration offers advantages over single-photoelectrode systems since it has the ability to increase cell photovoltage, making the dual-photoelectrode PFC an attractive option for solar fuel production, wastewater treatment, and environmental remediation applications.[7,13] For further details on the structural and operational principles of PFCs, readers are referred to recent comprehensive reviews.[11,12]

PFC characteristics are influenced by both the design and photoelectrode performance. H-type cells, extensively studied, feature a membrane separator to create distinct compartments for the photoanode and photocathode, preventing product crossover but increasing system complexity and cost. In contrast, membraneless configurations, such as microfluidic and single-cell PFCs, eliminate the need for membranes, reducing costs and simplifying the system. Microfluidic PFCs enhance molecule-electrode interactions,[8,9,14] while single-cell designs allow the photoanode and photocathode to be positioned either side by side or face to face, offering a low-cost alternative at the expense of some degree of product crossover.[15]

Regarding the photoelectrode, bismuth vanadate (BVO) is a potential photoanode thoroughly investigated for PEC water oxidation, among other target oxidation reactions.[16−18] Modifications have been proposed to increase the BVO photoactivity, such as heterojunction formation,[19] defect controlling,[20,21] doping,[22] and cocatalyst deposition.[18,21] A $BiVO_4/WO_3$ heterojunction film is a promising candidate for photoelectrochemical water splitting, specifically to increase charge separation in BVO.[23] For the $BiVO_4/WO_3$ heterojunction, electrons can travel from BVO to WO_3, while holes can migrate from the WO_3 to BVO. Therefore, the well-matched $BiVO_4/WO_3$ heterojunction efficiently drives the transport of the photogenerated carriers but still lacks improvements in the interfacial carriers' transfer resistance and surface defect passivation. Recently, one of us reported using a special band structure engineering with W-doped $BiVO_4$ (W:BVO) to form a ternary $W:BiVO_4/WO_3/V_2O_5$ heterojunction with increased photoactivity.[24] This photoanode presented increased visible light absorption and lesser charge recombination, where V_2O_5 facilitated the transport of holes and WO_3 additionally increased electron mobility.

Additionally, Cu-based photocathodes have garnered significant interest for CO_2RR due to their ability to efficiently convert CO_2 into carbon monoxide, formate, hydrocarbons, and alcohols.[25] Cuprous oxide (Cu_2O) with a band gap of ~2.2 eV[26] also possesses additional characteristics that make it suitable for various photocatalytic applications, particularly CO_2RR.[27−29] However, Cu_2O suffers from photocorrosion,[6] and various strategies have been employed to minimize this issue,[4] including morphological control,[30] the application of protective layers,[31] and junction manipulation.[32,33] The formation of a Cu_2O/CuO junction has proven effective in suppressing photocorrosion and enhancing the photocatalytic reaction, leading to improved efficiency and stability.[33] This synergy represents a significant advance toward more robust and sustainable photocatalytic technologies and marks a noteworthy contribution to the current scientific landscape.

In this work, we describe a novel, membraneless, and stationary PFC designed to spontaneously convert SO_3^{2-} and CO_2 into green fuels and electrical power under simulated solar illumination. Our system, featuring a unique shoulder-to-shoulder and dual-electrode configuration, consists of a $W:BiVO_4/WO_3/V_2O_5$ (W:BVO/WO/VO) photoanode and a Cu_2O/CuO photocathode, achieving an open-circuit photovoltage of 0.50 V and a short-circuit photocurrent of 0.50 mA cm^{-2} at one sun illumination (100 mW cm^{-2}, AM 1.5G). Notably, the system delivered a maximum power output of 0.05 mW cm^{-2}, the highest reported to date for a direct CO_2 PFC without noble metal-based catalysts. We systematically explore the anodic and cathodic reaction pathways both in half-cell experiments and within the operational device and the low-cost membraneless configuration, demonstrating enhanced CO_2 conversion efficiency coupled with sulfite oxidation. This work successfully achieves simultaneous CO_2 reduction and electricity generation without using exchange membranes, advancing sustainable and spontaneous solar-driven chemical fuel production.

https://doi.org/10.1021/acsaem.5c03695
ACS Appl. Energy Mater. 2026, 9, 2197−2208

2. EXPERIMENTAL SECTION

2.1. Synthesis of the Photoelectrodes

Fluorine-doped tin oxide (FTO)-coated glass substrates were employed and thoroughly cleaned by sequential treatments with detergent, deionized water, acetone, and isopropyl alcohol.

The photocathode (Cu_2O/CuO) was prepared via electrodeposition using a plating bath composed of 0.3 M copper sulfate (Sigma-Aldrich, 99.8%) and 3 M lactic acid (Sigma-Aldrich, 85% w/w) with the pH adjusted to 11 using NaOH.[33,34] FTO slides, limited to 1 cm^2, underwent Cu_2O electrodeposition at −0.8 mA cm^{-2} for 25 min using a CorrTest CS310 potentiostat at 40 °C. Platinum foil served as the counter electrode. After deposition, films were washed with water and ethanol and then annealed in air at 400 °C for 1 h to partially convert Cu_2O to CuO.

The photoanode (W:BVO/WO/VO) was prepared following previous reports.[24,35] Using a mass ratio of 2:1:1, powders of W:BVO_4 (2 mg), WO_3 (1 mg), and V_2O_5 (1 mg) were mixed and dispersed in 400 μL of isopropanol, followed by sonication for 2 h to ensure thorough mixing. The resulting suspension was then drop-cast onto FTO substrates with a 1 cm^2 geometric area. The films were subsequently annealed at 500 °C for 2 h in air to improve crystallinity and adhesion to the substrate. This three-phase heterojunction was chosen as a photoanode based on previous works highlighting the synergistic behavior of these materials in facilitating charge separation and transfer under ideal quantities, by balancing the light absorption capabilities of $BiVO_4$, enhancing electron mobility with WO_3, and facilitating hole mobility with V_2O_5.[24]

2.2. Characterization of the Photoelectrodes

The morphology and chemical properties of the electrodes were investigated using energy-dispersive X-ray spectroscopy (EDS) in a Zeiss Sigma scanning electron microscope coupled with a field emission gun (FEG). X-ray diffraction (XRD) was performed using a PANalytical Empyrean instrument with a Cu−Kα source. The XRD measurements were performed from 10 to 90° (Bragg−Brentano geometry) with a 3.2°/min scan speed. The step size and time per step were set at 0.013° and 60 s/step, respectively. UV−vis absorption measurements of the films were performed by using a Shimadzu UV-2600 spectrometer fitted with an integrating sphere. X-ray photoelectron spectroscopy (XPS) was used to elucidate the chemical surface composition of the samples. The analysis was carried out using an XPS spectrometer (Scienta-Omicron ESCA+) equipped with a high-performance hemispheric analyzer (EAC2000) and monochromatic Al K-α radiation (hν = 1486.6 eV) as an excitation source. The operating pressure was 10^{-9} Pa, and the high-resolution XPS spectra were recorded at a constant pass energy of 20 at 0.05 eV per step. The XPS spectra were calibrated using adventitious carbon (C 1s) at 284.8 eV. Curve fitting was preceded by data analysis using CasaXPS software and Shirley-type background subtraction. The thicknesses of the photoanode and photocathode films were determined by using a KLA Tencor P7 profilometer. Measurements were conducted with a scan rate of 50 μm per second and a sampling rate of 100 Hz. To ensure accuracy, 10 measurements were taken at different points on the sample and the values were averaged.

2.3. (Photo)electrochemical Measurements

Photoelectroactivity was examined using a CS310 CorrTest potentiostat, a solar simulator model 105000 from Abet Tech (150 W xenon lamp), and an AM1.5G filter. All measurements were calibrated using the reference solar cell model 15151 from Abet Tech to ensure a light intensity of 100 mW cm^{-2}. Half-cell linear sweep voltammetry (LSV) experiments were performed using a conventional three-electrode cell setup made of Teflon and quartz window, with and without light irradiation. For anodic half-cell measurements, three different N_2-saturated, aqueous electrolytes were evaluated: (i) 0.5 M Na_2SO_4 (pH 9), (ii) 0.5 M Na_2SO_4 + 0.5 M Na_2SO_3 (pH 9.7), and (iii) 0.5 M Na_2SO_4 + 0.5 M Na_2SO_3 + 0.04 M $NaHCO_3$ (pH 8.8). For the cathodic half-cell study, the same electrolyte solutions were tested under both N_2- and CO_2-saturated conditions to assess the impact of CO_2 on performance. It is worth noting that CO_2-saturated electrolytes presented a reduced pH of 6.7. LSV curves were obtained with potential scans ranging from −0.7 to 0.6 and 0.2 to −0.4 V *vs.* Ag/AgCl for the anodic and cathodic half-cell investigation with a step of 1 mV and a scan rate of 10 mV s^{-1} recorded. A platinum wire was employed as the counter electrode, while an Ag/AgCl electrode was the reference. The potentials referenced to Ag/AgCl were converted to the reversible hydrogen electrode (V_{RHE}) using the Nernst equation, as follows:[9] $V_{RHE} = V_{Ag/AgCl} + (0.059 \times pH) + 0.197$ V.

PFC polarization curves were obtained in a single-chamber reactor under stationary conditions with electrodes shoulder-by-shoulder (see Figure S1 for further details) using back illumination and W:BVO/WO/WO as the photoanode and Cu_2O/CuO as the photocathode. The electrolyte for PFC measurements was a 0.5 M Na_2SO_4 + 0.5 M Na_2SO_3 + 0.04 M $NaHCO_3$ solution with a saturated amount of CO_2 for 60 min. Polarization curves were recorded in potentiodynamic mode from the open-circuit voltage (V_{oc}) to 0 V, with a scan rate of 10 mV s^{-1}. Before each measurement, V_{oc} was allowed to stabilize until variations within the tolerance limit of 10 mV min^{-1} were reached.

To calculate the power density, the following equation was used:[36] $P = V \times J$. Chronoamperometry was performed at 0.35 V (point corresponding to 2/3 of maximum power in polarization curves) and at 0 V, conducted with a Metrohm potentiostat−galvanostat PGSTAT128N in a two-electrode setup, using a newly developed cell with a gastight cover to allow gas quantification (details in Figure S2). Prior to measurements, the reactor was saturated with high-purity CO_2 for 30 min (5 min at 4 mL min^{-1} followed by 25 min at 2 mL min^{-1}). A control test was conducted for 10 min in the dark (no products detected) and, subsequently, for 60 min under illumination (AM1.5 filter, 100 mW cm^{-2}). Gaseous products were analyzed every 20 min using an Agilent 7890B gas chromatograph (GC) equipped with flame ionization (FID) and thermal conductivity (TCD) detectors. The reactor outlet was directly connected to the GC through a stainless-steel line. CO_2 (99.999%) was used as the carrier gas at a constant flow rate of 1.0 mL min^{-1}, controlled by a mass flow controller. Gas samples were introduced via a fixed-volume sampling loop, corresponding to an injected volume of 0.99 mL per analysis. Gas separation was achieved using two columns connected in series: an HP-PLOT/Q column (40 m length, 0.53 mm internal diameter, and 40 μm film thickness) for the separation of CO_2, CO, and CH_4, followed by a molecular sieve column (30 m length, 0.53 mm internal diameter, and 40 μm film thickness) for the separation of H_2, O_2, and N_2. The GC oven was operated under isothermal conditions at 300 °C throughout the analysis. The injector temperature was set to 110 °C. Detector temperatures were 200 °C for the TCD and 300 °C for the FID. A methanizer operated at 380 °C was employed upstream of the FID for CO detection, with N_2 used as the FID makeup gas. The total chromatographic run time was 11 min, allowing the complete separation of all target gaseous species. Retention times and calibration curves for all analyzed gases were obtained using certified standard gas mixtures (White Martins, Brazil). Faradaic efficiencies (FE) for gaseous products were calculated based on the amount of charge associated with the formation of each product relative to the total charge passed during the reaction. The number of moles of each gaseous product (n_i) was determined from GC quantification using the corresponding calibration curves. The Faradaic efficiency for a given product i was then calculated using

$$FE_i(\%) = \frac{n_i \cdot z_i \cdot F}{Q} \times 100$$

where z_i is the number of electrons required to form one molecule of product i (8 for CH_4, 2 for H_2), F is the Faraday constant (96,485 C mol^{-1}), and Q is the total charge passed during the selected time interval, obtained by integrating the photocurrent−time curves.

2.4. Identification of Liquid Products from CO_2

For NMR analysis, 400 μL of the sample and 200 μL of deuterated water with TSP-d4 0.05% (w/v) were added to an NMR tube of 0.5 mm. ^{1}H NMR spectra were carried out on a Bruker Avance Neo

https://doi.org/10.1021/acsaem.5c03695
ACS Appl. Energy Mater. 2026, 9, 2197−2208

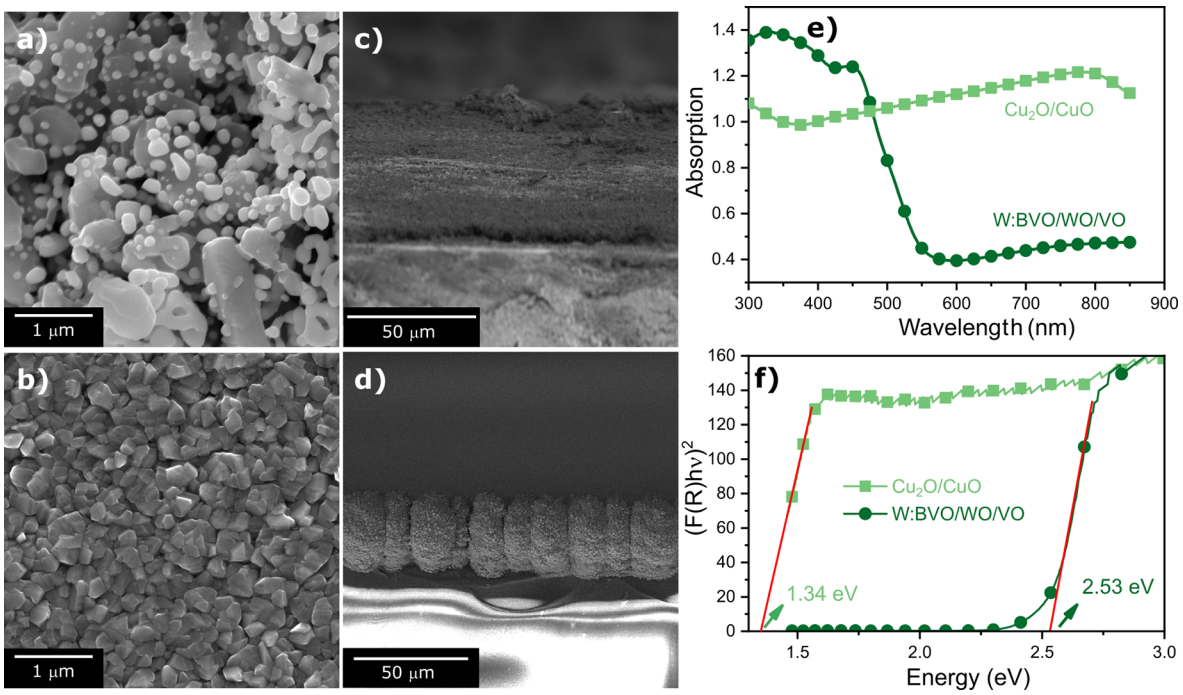

Figure 2. Morphological and optical characterization of the electrodes: representative top-view SEM images of (a) W:BVO/WO/VO and (b) Cu_2O/CuO. Representative cross-sectional view SEM images of (c) W:BVO/WO/VO and (d) Cu_2O/CuO. (e) UV−vis diffuse reflectance spectra and (f) Tauc plot of the photoelectrodes.

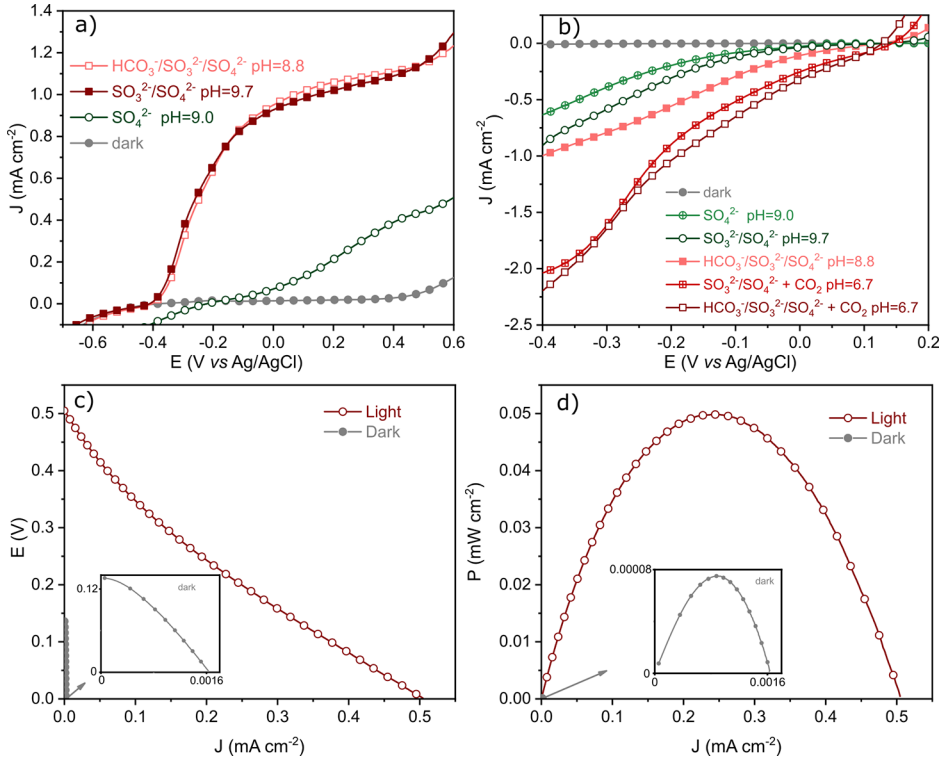

Figure 3. Photoelectrochemical tests using simulated solar irradiation (AM1.5G, 100 mW.cm^{-2}), a Ag/AgCl reference electrode, and a Pt counter electrode, with different electrolytes: (a) sulfite oxidation using the W:BVO/WO/VO photoanode and (b) CO_2 reduction using the Cu_2O/CuO photocathode. Full-cell measurements feature (c) polarization and (d) power density curves. Performance of the PFC (c, d) was obtained in the shoulder-by-shoulder configuration with a stationary two-electrode and single-compartment cell, employing W:BVO/WO/VO as the photoanode and Cu_2O/CuO as the photocathode. The electrolyte was 0.5 M Na_2SO_4 + 0.5 M Na_2SO_3 + 0.04 M $NaHCO_3$, with the CO_2 saturated for 60 min. Dark curves in panels (a) and (b) were obtained in the sulfate electrolyte for comparison. All other dark curves showed identical results without notable current generation.

https://doi.org/10.1021/acsaem.5c03695
ACS Appl. Energy Mater. 2026, 9, 2197−2208

(11.75 T) spectrometer, operating at 500 MHz for ^{1}H frequency. ^{1}H NMR spectra were acquired with 1 k scans (NS), 64 k points (TD), 2.62 s acquisition (AQ), a relaxation delay of 12 s (d1), and a spectral width (SW) of 25 ppm. NS and d1 values were adjusted to obtain a good signal-to-noise ratio. All spectra were processed using zero filling, an exponential multiplication of 1.0 Hz (LB), and manual phase and baseline corrections. Spiking tests using standard compounds were performed to corroborate the presence of the identified compounds in the sample. The relative proportion was calculated using the integral of the signals divided by the number of hydrogens present in each signal.

3. RESULTS AND DISCUSSION

The pristine W:BVO/WO/VO film surface reveals a complex structure with particles randomly dispersed on the FTO substrate, as shown in SEM images in Figure 2a. These particles exhibit diverse morphologies, encompassing spherical, rod-shaped, and plate-shaped structures, representing the W:BVO, VO, and WO components, respectively. This configuration establishes different heterojunctions within the material, as previously reported.[24] Figure 2b shows the SEM image of the pristine Cu_2O/CuO electrode, characterized by irregular and compacted truncated polyhedron-shaped particles. Figures 2c and 2d show cross-sectional views of the W:BVO/WO/VO and Cu_2O/CuO photoelectrodes, respectively. The profilometry of the photoanode and photocathode films shows mean thicknesses of 16.5 ± 0.5 and 3.5 ± 0.5 μm, respectively. The thicker photoanode film results from the drop-casting deposition of multiple-sized particles on the FTO (Figure 2a). The more uniform shape and size distribution of the Cu_2O/CuO particles obtained by electrodeposition fits better the particles on a film structure, generating a thinner and smoother film (Figure 2b).

Figure 2e illustrates that the photoanode can absorb light up to approximately 550 nm, whereas the photocathode can absorb light over the entire visible range. Previous research has reported the band gaps of V_2O_5, W:$BiVO_4$, and WO_3, prepared exactly as in this work, as 2.27, 2.44, and 2.90 eV, respectively.[24,35] Herein, the whole ternary composite photoanode exhibits a single band gap of 2.53 eV, as determined from the Tauc plot (Figure 2f). In contrast, as expected, the Cu_2O/CuO photocathode demonstrated a lower band gap of 1.34 eV.

Redox reactions at the electrolyte−electrode interface play a crucial role in photocurrents in a photoelectrochemical system. We conducted half-cell experiments to understand how each photoelectrode behaves under different electrochemical conditions. The results of these experiments are presented in Figure 3.

As shown in Figure 3a, the photoanode exhibited a photocurrent density of 0.4 mA cm^{-2} at 0.4 $V_{Ag/AgCl}$ during water oxidation when sulfate was the only component in the electrolyte. When sulfite was added to the electrolyte (sulfate/sulfite) at the same applied potential, the photocurrent increased from 0.4 to 1 mA cm^{-2}, more than doubling it. According to earlier research, the sulfite ion is a highly selective hole scavenger that facilitates effective charge transfer and photooxidation processes, resulting in enhanced photocurrents in anodic half-cells.[37] This result suggests that sulfite oxidation is a promising option as an inorganic fuel in a PFC. Additionally, the onset potential of the light-driven reaction was decreased by 0.25 V. On the other hand, the addition of carbonate ions does not significantly affect the PEC performance of the photoanode, indicating that the presence of these species in the electrolyte does not impact water/sulfite oxidation. This result is pivotal in allowing membraneless single-chamber PFCs for CO_2 reduction. Thus, the CO_2 fed in a cell will not react at the anodic surface, assuring that the active site of the photoanode exclusively participates in fuel oxidation.

In the cathodic half-cell investigation (Figure 3b), a photocurrent of −0.40 mA cm^{-2} at −0.3 $V_{Ag/AgCl}$ can be observed with only sulfate in the electrolyte. Interestingly, the addition of sulfite (sulfate/sulfite) slightly improved the efficiency of the photocathode, resulting in a slight increase in the photocurrent to −0.6 mA cm^{-2} at the same applied potential. Here, although sulfite can theoretically be reduced, it would occur at higher reducing potentials, near −0.86 V *vs.* Ag/AgCl at pH ∼9.7 (without CO_2).[38] This observation suggests that the increase in conductivity enhances current and/or that sulfite could act as a trap for holes created on the electrode surface and enhance the reduction process at the photocathode.[39] Adding bicarbonate (HCO_3^-) to the sulfite/sulfate electrolyte increases the cathodic current (Figure 3b), resulting in a photocurrent of ∼−0.8 mA cm^{-2} at −0.3 $V_{Ag/AgCl}$. Notably, the CO_2 was not externally saturated in the electrolyte in this case. Therefore, the photocurrent increase mostly comes from HCO_3^- reduction since it is the predominant species at pH 8.8, as indicated by the Bjerrum plot for carbonic acid derivatives.[40] Figure S3 presents the voltammograms on the RHE scale, for comparison. However, we emphasize that scale conversion may not account for interfacial pH variations.[41]

After saturating the sulfate/sulfite-based electrolyte with CO_2, the pH reduced from 8.8 to 6.7, and the photocurrent increased from −0.6 to −1.7 mA cm^{-2} at −0.3 $V_{Ag/AgCl}$. This result is a consequence of the CO_2 and bicarbonate (from CO_2) reduction reactions, since now both species may coexist according to the Bjerrum plot,[40] from here onward described solely as CO_2RR. Figure 3b also shows that the current is virtually constant by adding bicarbonate to a solution saturated with CO_2.

In summary, as shown in due course, the solution pH is initially alkaline and close to neutral after saturating with CO_2; thus, the CO_2RR is mostly controlled by the reduction of dissolved CO_2 and HCO_3^-. Regardless of the mechanism, the electrons—harvested from the anode and delivered to the cathode, and those directly generated through the photocathode light excitation—drive the conversion of CO_2 into products on the photocathode surface.[42−44] Therefore, these results highlight the potential of this electrolyte for use in shoulder-to-shoulder PFC systems for sustainable CO_2 conversion and utilization, demonstrating the importance of understanding the influence of electrolyte composition on the performance of both the photoanode and the photocathode in a PEC system.

A PFC works as a galvanic cell, generating cell voltage and electric work through a spontaneous redox reaction. The condition for spontaneity is governed by $\Delta G < 0$, as defined by $\Delta G = -nF\Delta E$, where n is the number of electrons transferred, F is Faraday's constant, and E is the cell voltage. A positive ΔE is crucial to ensure PFC functionality, indicating a spontaneous redox reaction that allows current flow and work production. In practical terms, the feasibility of PFC operation relies on the onset potential of the reduction reaction (E_{onset}^{C}) in the cathode surpassing that of the oxidation reaction (E_{onset}^{A}) in the anode, given by $(\Delta E) = E_{onset}^{C} - E_{onset}^{A}$.[7] Therefore,

https://doi.org/10.1021/acsaem.5c03695
ACS Appl. Energy Mater. 2026, 9, 2197−2208

Table 1. Compilation of the CO2RR PFC Performance under Different Configurations and with Distinct Electrodes[a]

system	electrode	condition	results	ref
dual-chamber, a proton membrane Nafion, flow	PC = Pt-coated carbon paper PA = TiO_2	anolyte is a CO_2-saturated mixture of deionized water, sulfuric acid, and methanol; the catholyte is a mixture of deionized water and sulfuric acid; UV-LED light source; 10 mW cm^{-2}	V_{OC} = 0.97 V J_{max} = 0.39 mA cm^{-2} P_{max} = 210 μW cm^{-2}	47
dual-chamber, cation-exchange membrane, rotating disc cathode	PC = Ti_3C_2 PA = TiO_2−NT	anolyte is 0.1 M Na_2SO_4 with methyl orange; the catholyte is a CO_2-saturated 0.1 M Na_2SO_4; two 8 W low-pressure Hg lamps (G8 T5, Philips) as a light source	V_{OC} = 0.80 V J_{max} = 0.70 mA cm^{-2} P_{max} = 28.50 μW cm^{-2}	48
dual-chamber, cation membrane, rotating disk electrode	PA = TiO_2−NT PC = Ti plate loaded with Ti_3C_2	electrolyte 0.1 M Na_2SO_4; anolyte pH = 13; catholyte with CO_2-saturated and pH = 1; irradiance not given	V_{OC} = 0.80 V J_{max} = 0.034 mA cm^{-2} P_{max} = 10.50 μW cm^{-2}	49
single-chamber, flow	PC = Pt-coated carbon paper PA = TiO_2	electrolyte is CO_2-saturated sulfuric acid; UV-LED lamp light source; 10 mW cm^{-2}	V_{OC} = 0.88 V J_{max} = 0.085 mA cm^{-2} P_{max} = 34 μW cm^{-2}	50
single-chamber, flow	PA = integrated system, which consists of a 3D TiO2/Ni foam and TiO_2 PC = Pt/carbon paper	electrolyte is CO_2-saturated 0.02 M H_2SO_4; UV-LED lamp light source; 10 mW cm^{-2}	V_{OC} = 0.98 V J_{max} = 0.20 mA cm^{-2} P_{max} = 122 μW cm^{-2}	51
single-chamber (shoulder-to-shoulder)	PA = W:BVO/WO/VO PC = Cu_2O/CuO	150 W Xe lamp, AM 1.5G, 100 mW cm^{-2}; the electrolyte is CO_2-saturated 0.5 M Na_2SO_4, 0.5 M Na_2SO_3, and 0.04 M $NaHCO_3$	V_{OC} = 0.50 V J_{max} = 0.50 mA cm^{-2} P_{max} = 50 μW cm^{-2}	this work

[a]PA = photoanode; PC = photocathode.

https://doi.org/10.1021/acsaem.5c03695
ACS Appl. Energy Mater. 2026, 9, 2197−2208

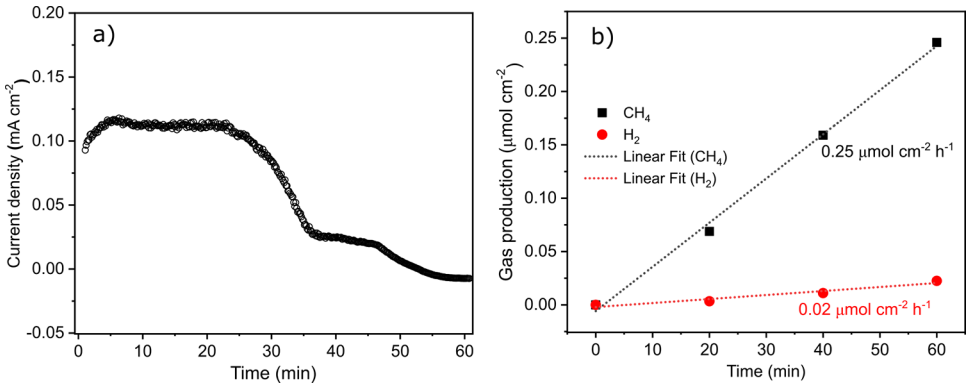

Figure 4. Photocurrent stability (a) and gas-phase product formation (b) during spontaneous CO_2 reduction in solar-driven PFC at 0 V.

assessing the onset potentials of the proposed oxidation and reduction reactions is essential to demonstrate PFC viability under realistic conditions.

The onset potentials identified from the derivative voltammetry of the reactions[45,46] in this study are shown in Figure S4. When coupling the illuminated W:BVO/WO/VO photoanode for sulfite oxidation with the Cu_2O/CuO photocathode for CO_2 reduction, the onset potentials are −0.41 and 0.15 V *vs.* Ag/AgCl (0.31 and 0.74 V *vs.* RHE), respectively. This results in a positive ΔE of 0.43 V, enabling spontaneous operation under illumination, where the device simultaneously generates electrical power and drives CO_2 reduction and sulfite oxidation in water. The spontaneous operation of the W:BVO/WO/VO-Cu_2O/CuO PFC arises from the combined photovoltage (net built-in potential) generated by the illuminated n-type and p-type semiconductors and the alignment of their band edges with the redox potentials of the coupled reactions.[7] Under illumination, the built-in electric fields at each semiconductor−electrolyte interface separate charge carriers, driving holes at the photoanode surface to oxidize sulfite and electrons at the photocathode to reduce CO_2. It allowed spontaneous charge transfer and product formation without an external voltage bias.

Consequently, PFC polarization and power density curves were obtained by assembling the two photoelectrodes in a shoulder-to-shoulder configuration under single-chamber stationary cell conditions (Figure S1). The polarization and power density curves are shown in Figures 3c and 3d, respectively. Under dark conditions, the performance is negligible with V_{OC} = 0.13 V and P_{max} = 0.08 μW cm^{-2}. These values significantly increased when the electrodes were exposed to light under a one sun condition. Specifically, the V_{OC} increased to ∼0.50 V, the P_{max} increased to 0.05 mW cm^{-2}, and the J_{max} reached 0.50 mA cm^{-2}.

Yu et al.[47] reported a PFC featuring a H-type cell, Nafion 211 membrane, flow conditions, TiO_2 as a photoanode, and commercial Pt-coated carbon paper (DMFC Cathode, Alfa Aesar, UK) as an air-breathing cathode. They investigated the PFC performance in using methanol as a fuel and anolyte saturated with CO_2 under acidic conditions, achieving a V_{OC} of 0.97 V, a J_{max} of 0.391 mA cm^{-2}, and a P_{max} of 0.207 mW cm^{-2} under a UV-LED illumination source (HTLD-S60-365, China). Zhang et al.[48] reported a similar PFC system but with a rotating Ti_3C_2 as a cathode and 0.1 M Na_2SO_4 + methyl orange solution as the electrolyte. They showed that wastewater is oxidized on the anodic side, producing CO_2 that was supplied to the cathodic chamber through a switchable gas channel. The CO_2 diffused into the cathode chamber was then further reduced at the cathode to produce CO and CH_4. The device achieved a V_{OC} of 0.80 V, a J_{max} of 0.70 mA cm^{-2}, and a P_{max} of 28.5 μW cm^{-2} using two 8 W low-pressure mercury lamps (G8 T5, Philips) as a light source. In another work,[49] a similar system with the same photoelectrodes was reported with some modifications, where 0.1 M Na_2SO_4 solution with CO_2 saturation was used as the catholyte (anolyte pH 13 and catholyte pH 1). The best results reached V_{OC} = 0.80 V, J_{max} = 0.34 mA cm^{-2}, and P_{max} = 10.50 μW cm^{-2}, with CH_4 as the main product.

Xie et al.,[50] constructed a flow PFC system consisting of the TiO_2 photoanode and Pt-coated carbon paper cathode, with the CO_2-saturated H_2SO_4 electrolyte. They showed CO_2 reduction to methanol and ethanol, achieving V_{OC} = 0.88 V, J_{max} = 0.08 mA cm^{-2}, and P_{max} = 0.03 mW cm^{-2}, using a UV-LED (HTLD-S60-365, China) as a light source. Jiao et al.[51] also reported CO_2 reduction to methanol and ethanol using a flow PFC comprising an integrated 3D TiO_2/Ni foam and TiO_2-coated FTO photoanode and commercial Pt/carbon paper as a cathode, with a CO_2-saturated 0.02 M H_2SO_4 electrolyte. They achieved a V_{OC} of 0.98 V, a J_{max} of 0.20 mA cm^{-2}, and a P_{max} of 0.122 mW cm^{-2} using a UV-LED (HTLD-S60-365, China, 10 mW cm^{-2}) as a light source.

Table 1 compiles key findings from related studies on the PFC performance for the CO_2RR under different configurations. After analyzing the data in Table 1, it becomes very difficult to establish a direct relationship between the results since some studies do not use light sources that match the solar spectrum, an important parameter for applications. Therefore, our results are comparable to the best works reported in Table 1, demonstrating enhanced photoelectrodes for solar energy conversion in a single-chamber, shoulder-to-shoulder, membraneless, and stationary PFC configuration.

3.1. Liquid and Gas Product Identification from CO_2 Reduction

After all half-cell experiments and the two-electrode polarization studies, potentiostatic experiments were performed at 0 V (unbiased, Figure 4) and 0.35 V (2/3 of the maximum power density produced by the PFC, Figure S5) for 1 h. Gas quantification was conducted using online GC every 20 min in a specially designed cell with a gastight cover (Figure S2). Subsequently, aliquots from the electrolyte were collected after 1 h and subjected to ^{1}H NMR analysis to identify the CO_2RR liquid products. As shown in Figure 4a, the device operated at 0 V exhibited an initial photocurrent density of ∼0.12 mA

https://doi.org/10.1021/acsaem.5c03695
ACS Appl. Energy Mater. 2026, 9, 2197−2208

cm^{-2}, which remained stable for approximately 25 min before gradually declining to ~0.03 mA cm^{-2} at 35 min. This decrease is attributed to photocorrosion of the Cu_2O-based photocathode (discussed later). After this point, the photocurrent continued to decrease, reaching nearly zero at ~50 min. Figure 4b presents the corresponding gas-phase products detected over time. CO_2 was selectively reduced to CH_4 at a rate of 0.25 μmol cm^{-2} h^{-1}, while proton reduction yielded H_2 at trace quantities of 0.02 μmol cm^{-2} h^{-1}. Faradaic efficiencies, calculated in the first 20 min (0.13 C of total charge), prior to a significant photocurrent drop, were 40.8% for CH_4 and 0.5% for H_2. These results demonstrate that CO_2 reduction overwhelmingly dominates over the competing water reduction pathway under the applied conditions.

The ^{1}H NMR spectral profiles of the samples displayed characteristic signals of ethanol, acetate (CH_3COO^-), methanol, and formate ($HCOO^-$), alongside a few unidentified compound signals in a lesser proportion (Figure S6). All identified compounds were annotated using standard addition experiments (spiking). The identified compounds are present in low concentration owing to a high proportion of water from the reaction medium, and their detailed relative proportions are presented in Table 2. Consequently, it can be observed that the predominant compound formed was ethanol, followed by formate, acetate, and methanol.

Table 2. Relative Proportion of Identified Liquid Compounds Using NMR

compound	^{1}H NMR chemical shift (ppm)	assignment (number of H)	relative proportion[a]
formate	8.46	HCOOH (1)	1.0
methanol	3.37	CH_3 (3)	0.56
acetate	1.93	CH_3 (3)	0.95
ethanol	1.19	CH_3 (3)	1.4

[a]Calculated by dividing the integral values from the ^{1}H NMR spectrum by the number of hydrogens in each signal.

The unprotonated formate is found instead of formic acid due to pH 6.7 of the product solution since the pK_a of the acid is 3.77. Carbonate may be directly reduced to formate in a half-reaction involving two electrons. Although bicarbonate is not likely to reduce in the presence of carbonate, as shown by the differences in E_R^0 and the voltammograms in Figure 3b, some small amount of such anions could be reduced to formate as well since we cannot distinguish whether formate originates from carbonate or bicarbonate reduction reaction. Methanol and ethanol are protonated at pH 6.7 due to their pK_a 15.5 and 15.9, respectively. Considering that the pK_a of acetic acid is 4.75, the product found here is unprotonated at pH 6.7.

Our study presents a dual PFC system that effectively captures and converts CO_2 into high-value compounds without needing external bias. While the current output power of our PFC ranks among the highest reported in the literature under one sun conditions (AM1.5G, 100 mW cm^{-2}), integrating the photocatalysts into a membraneless configuration showcases significant potential in tackling the issue of CO_2 mitigation. To optimize both product yield and conversion efficiency, exploiting convective mass transport within a flow-through electrode setup could be advantageous. This approach can enhance collision rates between reactants and catalyst surfaces, potentially boosting overall performance.

3.2. Discussion of Photoelectrode Stability and Surface Composition

XPS analysis was performed to better understand the chemical processes occurring on the sample surface. Measurements were performed before and after the PFC experiment. The XPS data are displayed in Figure S7. For C 1s, four components were shown at approximately 284.8, 285.8 (±0.2), 287.0 (±0.2), and 288.8 (±0.1) eV, attributed to the C−C, C−OH (or C−O−C), C=O, and O−C=C bonds, respectively. These contributions come from adventitious carbon; the main peak was used for energy calibration.

The high-resolution spectrum of the as-prepared photoanode was deconvoluted into four distinct components, Figure S7a. At 530.0 ± 0.1 eV, the main peak comes from oxygen atoms bound to metals in the lattice structure.[18,52] Since the photoanode comprises three distinct oxides, isolating each metal−oxygen signal proves challenging. Additionally, the peak at 530.9 eV is ascribed to adsorbed hydroxyl groups on the surface (HO^-), and the 531.9 and 533.0 eV peaks are attributed to carbon surface contaminations from C−OH and C−O−C (or O−C−C), respectively.[53,54] The W 4f spectra showed two peaks positioned at 35.7 and 37.7 eV and attributed to W^{6+}, Figure S7b.[55] The Bi 4f spectrum shows two peaks located at 164.4 and 159.0 eV, with an energy separation of 5.3 eV, Figure S7c. The V 2p spectrum shows two peaks at 524.0 and 516.6 eV, with an energy separation of 7.4 eV, Figure S7d. It indicates that the bismuth and vanadium species are in the trivalent and pentavalent states, respectively.[9,18] The photoanode surface composition was investigated after PFC operation under light irradiation (AM1.5G, 100 mW cm^{-2}). After PFC tests, the photoanode's Bi 4f and V 2p peaks showed a 0.2 and 0.3 eV shift to lower binding energy, respectively. For O 1s, the shift was 0.1 eV in the same direction. W 4f signal decreased after PFC operation, making it difficult to ensure a chemical shift. These results indicate that the surface composition is only slightly affected after the electrode is exposed to the operating conditions. Details of peak component fittings can be accessed in Table S1.

Figure 5 shows the O 1s and Cu 2p high-resolution XPS spectra of the Cu_2O/CuO photocathode for investigating its chemical surface composition before and after PFC operation. The as-obtained photocathode showed five O 1s peaks located at 529.8 eV (48.43%), 530.7 eV (15.76%), 531.5 eV (19.32%), 532.2 eV (9.90%), and 533.2 eV (6.59%), as shown in Figure 5a. The first two peaks can be assigned to Cu−O bonding in CuO and $Cu(OH)_2$ lattice, respectively.[56−58] The peak at 531.5 eV is ascribed to HO^-; the other peaks at 532.2 and 533.2 eV are attributed to surface contaminations from C−OH and C−O−C (or O−C−C).[59] After irradiation, the $Cu(OH)_2$ and HO^- contents were practically the same, but carbon-based contaminations increased in the latter case, see Table S2.

The Cu 2p high-resolution spectra showed two doublets in the spectrum and their associated satellites, characteristics of Cu^{2+}, as shown in Figure 5b. One doublet shows two peaks centered at 933.6 and 953.4 eV, which is assigned to the Cu $2p_{3/2}$ and Cu $2p_{1/2}$ from CuO, respectively.[57,58] These peaks contribute 79.6% of the Cu 2p spectrum. The other 20.4% comes from the doublet centered at 934.9 and 955.4 eV, evidencing the formation of $Cu(OH)_2$.[57,58] As can be seem, Cu_2O was not found on the photocathode surface, which is expected since the electrodes were calcined at 400 °C for the Cu_2O/CuO heterojunction formation. It is important to highlight that the Cu 2p spectra before and after PFC

https://doi.org/10.1021/acsaem.5c03695
ACS Appl. Energy Mater. 2026, 9, 2197−2208

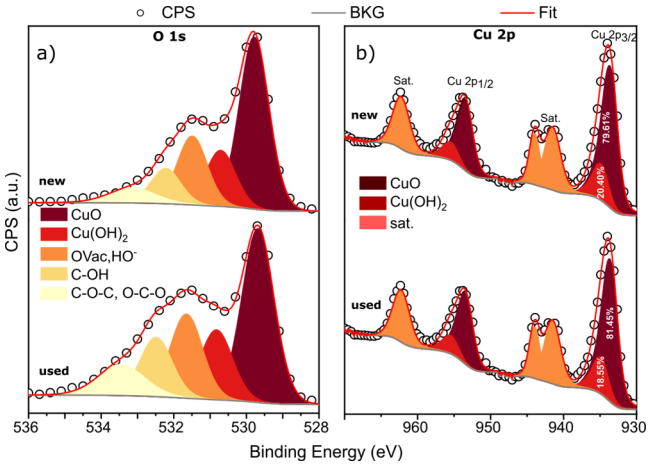

Figure 5. High-resolution XPS spectra of the Cu_2O/CuO photocathode before and after irradiation under PFC operating conditions: (a) O 1s and (b) Cu 2p regions. All spectra were adjusted using a Shirley background and GL(30) and DS(0.25,500,8) line shapes for O 1s and Cu 2p, respectively. The O 1s and Cu 2p components were constrained to the same fwhm, except for the (C−O−C/O−C−C) contribution, for which we allowed a 50% variation. The area of the Cu 2p doublets was constrained as expected.

operation are almost identical with similar surface contributions. The CuO and $Cu(OH)_2$ peaks shifted 0.1 and 0.2 eV to the lower binding energy direction, respectively (Table S2).

The XRD patterns and optical characterization of the samples are presented in Figure S8. The photoanode presents diffraction peaks corresponding to the expected crystalline phases (BVO, WO, and VO), Figure S8a.[24,35] Conversely, the photocathode's XRD data are displayed in Figure S8b. After the peaks associated with FTO are discarded, the most prominent peaks associated with Cu_2O in the cubic phase (crystallography open database—COD, 9005769) are those located at around 29.5, 36.3, 42.3, and 61.2°. The remaining peaks are indexed to CuO in the monoclinic phase (COD 1011194). These photocathode XRD data confirm the expected Cu_2O/CuO composition. The XRD data further confirm that the photoanode structural properties did not drastically change after the PFC operation. However, this was not the case with the photocathode. As shown in Figure S8b, the peaks from Cu_2O, estimated around 30, 36, 43, and 61°, disappeared, indicating a complete oxidation of Cu_2O to CuO after PFC operation. Drastic changes in the morphology of the photocathode can also be observed, as shown in Figure S9.

As already mentioned, the drawback of copper-based photocathodes is photocorrosion. Wang et al.[6] investigated photocorrosion under diverse conditions to comprehensively elucidate the corrosion mechanism of Cu_2O and its influencing factors. Their findings underscored the pivotal role of accumulated photogenerated electrons in Cu_2O corrosion, attributable to the sluggish kinetics of the carbon dioxide reduction reaction on the Cu_2O surface. The authors highlighted the efficacy of electron sacrificial agents in reducing corrosion by promoting the immediate electron consumption. Additionally, their work revealed that oxygen aids in corrosion reduction, enhancing the electron utilization efficiency.

Given that photogenerated electrons (e^-) at the photocathode/electrolyte interface likely participate in CO_2 reduction, while the resulting holes (h^+) may recombine at the photocathode/substrate interface with e^- coming from the photoanode, a plausible mechanism arises: the quantity of generated electrons might not completely neutralize all formed h^+. In such a scenario, residual h^+ could theoretically initiate oxidation processes at the photocathode/substrate interface. This speculative explanation implies a potential correlation between the availability of e^- from the external circuit and the photocathode stability, underscoring the intricate interactions within the photocatalytic system.

Undoubtedly, a thorough investigation into stability mechanisms is imperative to fully follow the oxidation phenomenon's impact on the sample's performance. However, this aspect currently awaits further exploration in future research endeavors. A deeper comprehension of the interplay between oxidative processes and material stability holds promise for refining strategies to optimize the photocathode's functionality.

4. CONCLUSIONS

We investigated for the first time a stationary, single-chamber, membraneless, solar-driven fuel cell system for CO_2 reduction and sulfite oxidation employing two light-sensitive semiconductor-based electrodes. The photocathode and photoanode were specifically designed to have improved photoelectroactivity for CO_2 reduction and sulfite oxidation, respectively, converting solar light into electrical energy and green liquid fuels spontaneously. Different electrolyte compositions were tested using half-cell measurements, showing that the combination of Na_2SO_4, Na_2SO_3, and $NaHCO_3$ offered better conditions for the CO_2 reduction reaction in a single-compartment PFC.

The W:$BiVO_4$/WO_3/V_2O_5 photoanode showed outstanding photoactivity, initiating sulfite oxidation at −0.4 V *vs.* Ag/AgCl and showed a photocurrent density of 1.0 mA cm^{-2} at 0.4 V *vs.* Ag/AgCl. The photocathode started CO_2 photoreduction at 0.15 V *vs.* Ag/AgCl and presented a photocurrent density of 1.7 mA cm^2 at −0.3 V *vs.* Ag/AgCl. The photocathode and photoanode combination showed a theoretical V_{OC} of 0.56 V for coupled CO_2 reduction and sulfite oxidation. Under simulated sunlight exposure, the shoulder-to-shoulder, single-compartment, and membraneless PFC demonstrated an experimental V_{OC} of 0.50 V and a short-circuit current of 0.5 mA cm^{-2}, resulting in a maximum power output of 0.05 mW cm^{-2}. The small deviation from the experimental V_{OC} to the theoretical value is attributed to low internal losses.

Following PFC operation, the device selectively converted CO_2 into CH_4 in the gas phase, while only trace amounts of H_2 were detected, confirming minimal competition from water reduction. In the liquid phase, ethanol, formate, acetate, and methanol were formed with ethanol showing the highest relative selectivity among these products. These results demonstrate that the proposed PFC can generate C1−C2 green fuels while simultaneously producing renewable energy under simulated sunlight despite gradual photocathode degradation over time.

■ ASSOCIATED CONTENT

Supporting Information

The Supporting Information is available free of charge at https://pubs.acs.org/doi/10.1021/acsaem.5c03695.

Details of the reactor for PFC without (Figure S1) and with (Figure S2) gas sampling, LSV curves on the RHE scale (Figure S3), voltammograms and their derivative

https://doi.org/10.1021/acsaem.5c03695
ACS Appl. Energy Mater. 2026, 9, 2197−2208

curves (Figure S4), stability test of two-photoelectrode PFC operated at 0.35 V—2/3 of the maximum power density (Figure S5), ^{1}H NMR spectrum (Figure S6); high-resolution XPS spectrum (Figure S7), DRX (Figure S8), morphological characterization of the electrodes after PFC operation (Figure S9), XPS data fitting of the photoanode (Table S1), and XPS data fitting of the photocathode (Table S2) (PDF)

AUTHOR INFORMATION

Corresponding Authors

Luiz Eduardo Gomes − *Laboratory of Advanced Technologies in Energy and Sustainability (LATES), Institute of Physics, Federal University of Mato Grosso do Sul, Campo Grande, MS 79070-900, Brazil*; Email: luiz.eduardo@ufms.br

Heberton Wender − *Laboratory of Advanced Technologies in Energy and Sustainability (LATES), Institute of Physics, Federal University of Mato Grosso do Sul, Campo Grande, MS 79070-900, Brazil*; orcid.org/0000-0002-1417-3581; Email: heberton.wender@ufms.br

Authors

Bárbara A.C. Sá − *Institute of Science, Engineering, and Technology, Federal University of Jequitinhonha and Mucuri Valleys (UFVJM), Teófilo Otoni 39803-371, Brazil*

Márcio C. Pereira − *Institute of Science, Engineering, and Technology, Federal University of Jequitinhonha and Mucuri Valleys (UFVJM), Teófilo Otoni 39803-371, Brazil*; orcid.org/0000-0001-9143-782X

Luiz Felipe Plaça − *Laboratory of Advanced Technologies in Energy and Sustainability (LATES), Institute of Physics, Federal University of Mato Grosso do Sul, Campo Grande, MS 79070-900, Brazil*

Maximiliano J. M. Zapata − *Laboratory of Advanced Technologies in Energy and Sustainability (LATES), Institute of Physics, Federal University of Mato Grosso do Sul, Campo Grande, MS 79070-900, Brazil*

Mohammed A. M. Bajiri − *São Carlos Institute of Physics, University of São Paulo, IFSC−USP, São Carlos, SP 13566-590, Brazil*; orcid.org/0000-0002-3961-7484

Niqab Khan − *São Carlos Institute of Physics, University of São Paulo, IFSC−USP, São Carlos, SP 13566-590, Brazil*

Glaucia B. Alcantara − *Institute of Chemistry, Federal University of Mato Grosso do Sul, Campo Grande, MS 79070-900, Brazil*

André Luis de Jesus Pereira − *Laboratório de Plasmas e Processos (LPP), Instituto Tecnológico de Aeronáutica (ITA), São José dos Campos 12228-900, Brazil*; orcid.org/0000-0003-4757-8080

Renato V. Gonçalves − *São Carlos Institute of Physics, University of São Paulo, IFSC−USP, São Carlos, SP 13566-590, Brazil*; orcid.org/0000-0002-3372-6647

Cauê A. Martins − *Laboratory of Advanced Technologies in Energy and Sustainability (LATES), Institute of Physics, Federal University of Mato Grosso do Sul, Campo Grande, MS 79070-900, Brazil*; orcid.org/0000-0003-3634-0624

Complete contact information is available at: https://pubs.acs.org/10.1021/acsaem.5c03695

Funding

The Article Processing Charge for the publication of this research was funded by the Coordenacao de Aperfeicoamento de Pessoal de Nivel Superior (CAPES), Brazil (ROR identifier: 00x0ma614).

Notes

The authors declare no competing financial interest.

ACKNOWLEDGMENTS

This work was partially supported by the National Council for Scientific and Technological Development (CNPq: processes # 313300/2020-8, # 408066/2022-9, # 409402/2023-0, # 303726/2021-0, and # 400013/2023-1) and The Foundation for Support to the Development of Teaching, Science, and Technology of the State of Mato Grosso do Sul (FUNDECT: project # 180/2023, # 228/2022, and # 028/2022). The authors also acknowledge the financial support provided by the CAPES-PrInt funding program (grants 88881.311921/2018-01 and 88887.311920/2018-00) and the São Paulo Research Foundation (FAPESP: grant no. 2022/02994-2). This study was supported by the Universidade Federal de Mato Grosso do Sul—UFMS/MEC—Brasil and financed in part by the Coordenação de Aperfeiçoamento de Pessoal de Nível Superior—Brasil (CAPES)—Finance Code 001. We also gratefully acknowledge the support of the RCGI − Research Centre for Greenhouse Gas Innovation, hosted by the University of São Paulo (USP) and sponsored by FAPESP − São Paulo Research Foundation (2020/15230-5) and Shell Brasil, and the strategic importance of the support given by ANP (Brazil's National Oil, Natural Gas, and Biofuels Agency) through the R&D levy regulation.

REFERENCES

(1) Dey, S.; Naidu, B. S.; Rao, C. N. R. Beneficial Effects of Substituting Trivalent Ions in the B-Site of La0.5Sr0.5Mn1−xAxO3 (A = Al, Ga, Sc) on the Thermochemical Generation of CO and H2 from CO2 and H2O. *Dalton Trans* **2016**, *45* (6), 2430−2435.

(2) Nitopi, S.; Bertheussen, E.; Scott, S. B.; Liu, X.; Engstfeld, A. K.; Horch, S.; Seger, B.; Stephens, I. E. L.; Chan, K.; Hahn, C.; Nørskov, J. K.; Jaramillo, T. F.; Chorkendorff, I. Progress and Perspectives of Electrochemical CO_2 Reduction on Copper in Aqueous Electrolyte. *Chem. Rev.* **2019**, *119* (12), 7610−7672.

(3) Fu, J.; Jiang, K.; Qiu, X.; Yu, J.; Liu, M. Product Selectivity of Photocatalytic CO2 Reduction Reactions. *Mater. Today* **2020**, *32*, 222−243.

(4) Chen, S.; Huang, D.; Xu, P.; Xue, W.; Lei, L.; Cheng, M.; Wang, R.; Liu, X.; Deng, R. Semiconductor-Based Photocatalysts for Photocatalytic and Photoelectrochemical Water Splitting: Will We Stop with Photocorrosion? *J. Mater. Chem. A* **2020**, *8* (5), 2286−2322.

(5) Li, C.; Guo, R.; Zhang, Z.; Wu, T.; Pan, W. Converting CO_2 into Value-Added Products by Cu_2O-Based Catalysts: From Photocatalysis, Electrocatalysis to Photoelectrocatalysis. *Small* **2023**, *19* (19), 2207875.

(6) Wang, Q.; Zhang, Y.; Liu, Y.; Wang, K.; Qiu, W.; Chen, L.; Li, W.; Li, J. Photocorrosion Behavior of Cu2O Nanowires during Photoelectrochemical CO2 Reduction. *J. Electroanal. Chem.* **2022**, *912*, No. 116252.

(7) Queiroz, B. D.; Fernandes, J. A.; Martins, C. A.; Wender, H. Photocatalytic Fuel Cells: From Batch to Microfluidics. *J. Environ. Chem. Eng.* **2022**, *10* (3), No. 107611.

(8) Plaça, L. F.; Vital, P.-L. S.; Gomes, L. E.; Roveda, A. C.; Cardoso, D. R.; Martins, C. A.; Wender, H. Black TiO_2 Photoanodes for Direct Methanol Photo Fuel Cells. *ACS Appl. Mater. Interfaces* **2023**, *15* (37), 43259−43271.

(9) Guima, K.-E.; Gomes, L. E.; Alves Fernandes, J.; Wender, H.; Martins, C. A. Harvesting Energy from an Organic Pollutant Model

Using a New 3D-Printed Microfluidic Photo Fuel Cell. *ACS Appl. Mater. Interfaces* **2020**, *12* (49), 54563−54572.
(10) Nielander, A. C.; Shaner, M. R.; Papadantonakis, K. M.; Francis, S. A.; Lewis, N. S. A Taxonomy for Solar Fuels Generators. *Energy Environ. Sci.* **2015**, *8* (1), 16−25.
(11) Wu, Y.-C.; Song, R.-J.; Li, J.-H. Recent Advances in Photoelectrochemical Cells (PECs) for Organic Synthesis. *Org. Chem. Front.* **2020**, *7*, 1895.
(12) He, Y.; Chen, K.; Leung, M. K. H.; Zhang, Y.; Li, L.; Li, G.; Xuan, J.; Li, J. Photocatalytic Fuel Cell − A Review. *Chem. Eng. J.* **2022**, *428*, No. 131074.
(13) Dhawle, R.; Vakros, J.; Dracopoulos, V.; Manariotis, I. D.; Mantzavinos, D.; Lianos, P. Enhancement of the Photoelectrochemical Production of Hydrogen Peroxide under Intermittent Light Supply in the Presence of an Optimized Biochar Supercapacitor. *Electrochim. Acta* **2022**, *427*, No. 140846.
(14) He, Y.; Zhang, Y.; Li, L.; Shen, W.; Li, J. An Efficient Optofluidic Photocatalytic Fuel Cell with Dual-Photoelectrode for Electricity Generation from Wastewater Treatment. *J. Solid State Chem.* **2021**, *293*, No. 121780.
(15) Song-Can, W. A. N. G.; Feng-Qiu, T. A. N. G.; Lian-Zhou, W. A. N. G. Visible Light Responsive Metal Oxide Photoanodes for Photoelectrochemical Water Splitting: A Comprehensive Review on Rational Materials Design. *J. Inorg. Mater.* **2018**, *33* (2), 173.
(16) Khan, N.; Stelo, F.; Santos, G. H. C.; Rossi, L. M.; Gonçalves, R. V.; Wender, H. Recent Advances on Z-Scheme Engineered BiVO4-Based Semiconductor Photocatalysts for CO2 Reduction: A Review. *Appl. Surf. Sci. Adv.* **2022**, *11*, No. 100289.
(17) Shi, X.; Zhang, Y.; Siahrostami, S.; Zheng, X. Light-Driven $BiVO_4$ Fuel Cell with Simultaneous Production of H_2O_2. *Adv. Energy Mater.* **2018**, *8* (23), 1801158.
(18) Gomes, L. E.; Nogueira, A. C.; da Silva, M. F.; Plaça, L. F.; Maia, L. J. Q.; Gonçalves, R. V.; Ullah, S.; Khan, S.; Wender, H. Enhanced Photocatalytic Activity of BiVO4/Pt/PtOx Photocatalyst: The Role of Pt Oxidation State. *Appl. Surf. Sci.* **2021**, *567*, No. 150773.
(19) Gao, L.; Zhou, Y.; Cao, L.; Cao, Y.; Zhang, H.; Zhang, M.; Yin, H.; Ai, S. Photoelectrochemical Sensor for Histone Deacetylase Sirt1 Detection Based on Z-Scheme Heterojunction of CuS−BiVO4 Photoactive Material and the Cyclic Etching of MnO2 by NADH. *Talanta* **2024**, *268*, No. 125307.
(20) Tolod, K. R.; Saboo, T.; Hernández, S.; Guzmán, H.; Castellino, M.; Irani, R.; Bogdanoff, P.; Abdi, F. F.; Quadrelli, E. A.; Russo, N. Insights on the Surface Chemistry of BiVO4 Photoelectrodes and the Role of Al Overlayers on Its Water Oxidation Activity. *Appl. Catal. A Gen.* **2020**, *605*, No. 117796.
(21) Mane, P.; Burungale, V.; Bae, H.; Seong, C.; Heo, J.; Kang, S. H.; Ha, J.-S. Integration of Surficial Oxygen Vacancies and Interfacial Two-Dimensional NiFe-Layered Double Hydroxide Nanosheets onto Bismuth Vanadate Photoanode for Boosted Photoelectrochemical Water Splitting. *J. Power Sources* **2024**, *591*, No. 233832.
(22) Guan, Y.; Gu, X.; Deng, Q.; Wang, S.; Li, Z.; Yan, S.; Zou, Z. Synergy Effect of the Enhanced Local Electric Field and Built-In Electric Field of CoS/Mo-Doped $BiVO_4$ for Photoelectrochemical Water Oxidation. *Inorg. Chem.* **2023**, *62* (41), 16919−16931.
(23) Liu, C.; Yang, Y.; Li, J.; Chen, S.; Li, W.; Tang, X. An in Situ Transformation Approach for Fabrication of BiVO4/WO3 Heterojunction Photoanode with High Photoelectrochemical Activity. *Chem. Eng. J.* **2017**, *326*, 603−611.
(24) Andrade, T. S.; Sá, B. A. C.; Oliveira, A. T.; Bruziquesi, C. G. O.; Salomão, P. E. A.; Rodriguez, M.; Nogueira, F. G. E.; Alves de Oliveira, L. C.; Pereira, M. C. W BiVO4-WO3-V2O5 Heterostructures Increase Light Absorption and Charge Transport in Photoanodes for Water Splitting. *J. Environ. Chem. Eng.* **2022**, *10* (2), No. 107278.
(25) Chang, X.; Wang, T.; Zhang, P.; Wei, Y.; Zhao, J.; Gong, J. Stable Aqueous Photoelectrochemical CO_2 Reduction by a Cu_2O Dark Cathode with Improved Selectivity for Carbonaceous Products. *Angewe. Chem., Int. Ed.* **2016**, *55* (31), 8840−8845.
(26) Rej, S.; Bisetto, M.; Naldoni, A.; Fornasiero, P. Well-Defined Cu2O Photocatalysts for Solar Fuels and Chemicals. *J. Mater. Chem. A* **2021**, *9* (10), 5915−5951.
(27) Kalamaras, E.; Belekoukia, M.; Tan, J. Z. Y.; Xuan, J.; Maroto-Valer, M. M.; Andresen, J. M. A Microfluidic Photoelectrochemical Cell for Solar-Driven CO2 Conversion into Liquid Fuels with CuO-Based Photocathodes. *Faraday Discuss.* **2019**, *215* (0), 329−344.
(28) Kahsay, A. W.; Ibrahim, K. B.; Tsai, M. C.; Birhanu, M. K.; Chala, S. A.; Su, W. N.; Hwang, B. J. Selective and Low Overpotential Electrochemical CO 2 Reduction to Formate on CuS Decorated CuO Heterostructure. *Catal. Lett.* **2019**, *149* (3), 860−869.
(29) Ávila-López, M. A.; Gavrielides, S.; Luo, X.; Ojoajogwu, A. E.; Tan, J. Z. Y.; Luévano-Hipólito, E.; Torres-Martínez, L. M.; Maroto-Valer, M. M. Comparative Study of CO2 Photoreduction Using Different Conformations of CuO Photocatalyst: Powder, Coating on Mesh and Thin Film. *J. CO2 Util.* **2021**, *50*, No. 101588.
(30) Zheng, Y.; Duan, Z.; Liang, R.; Lv, R.; Wang, C.; Zhang, Z.; Wan, S.; Wang, S.; Xiong, H.; Ngaw, C. K.; Lin, J.; Wang, Y. Shape-Dependent Performance of Cu/Cu_2O for Photocatalytic Reduction of CO_2. *ChemSusChem* **2022**, *15* (10), No. e202200216.
(31) Akbar, M. B.; Gong, Y.; Wang, Y.; Woldu, A. R.; Zhang, X.; He, T. Role of TiO_2 Coating Layer on the Performance of Cu_2O Photocathode in Photoelectrochemical CO_2 Reduction. *Nanotechnology* **2021**, *32* (39), 395707.
(32) An, X.; Li, K.; Tang, J. Cu2O/Reduced Graphene Oxide Composites for the Photocatalytic Conversion of CO2. *ChemSusChem* **2014**, *7* (4), 1086−1093.
(33) Panzeri, G.; Cristina, M.; Jagadeesh, M. S.; Bussetti, G.; Magagnin, L. Modification of Large Area Cu2O/CuO Photocathode with CuS Non-Noble Catalyst for Improved Photocurrent and Stability. *Sci. Rep.* **2020**, *10* (1), 1−10.
(34) Paracchino, A.; Brauer, J. C.; Moser, J. E.; Thimsen, E.; Graetzel, M. Synthesis and Characterization of High-Photoactivity Electrodeposited Cu2O Solar Absorber by Photoelectrochemistry and Ultrafast Spectroscopy. *J. Phys. Chem. C* **2012**, *116* (13), 7341−7350.
(35) Oliveira, A. T.; Rodriguez, M.; Andrade, T. S.; de Souza, H. E. A.; Ardisson, J. D.; Oliveira, H. S.; Oliveira, L. C. A.; Lorençon, E.; Silva, A. C.; Nascimento, L. L.; Patrocínio, A. O. T.; Pereira, M. C. High Water Oxidation Performance of W-Doped $BiVO_4$ Photoanodes Coupled to V_2O_5 Rods as a Photoabsorber and Hole Carrier. *Solar RRL* **2018**, *2* (8), 1800089.
(36) Ghorbani, M.; Solaimany Nazar, A. R.; Farhadian, M.; Tangestaninejad, S. Efficient Tetracycline Degradation and Electricity Production in Photocatalytic Fuel Cell Based on ZnO Nanorod/BiOBr/UiO-66-NH2 Photoanode and Cu2O/CuO Photocathode. *Energy* **2023**, *272*, No. 127114.
(37) Yu, J. M.; Lee, J.; Kim, Y. S.; Song, J.; Oh, J.; Lee, S. M.; Jeong, M.; Kim, Y.; Kwak, J. H.; Cho, S.; Yang, C.; Jang, J.-W. High-Performance and Stable Photoelectrochemical Water Splitting Cell with Organic-Photoactive-Layer-Based Photoanode. *Nat. Commun.* **2020**, *11* (1), 5509.
(38) Beschkov, V.; Razkazova-Velkova, E.; Martinov, M.; Stefanov, S. Electricity Production from Marine Water by Sulfide-Driven Fuel Cell. *Appl. Sci.* **2018**, *8* (10), 1926.
(39) Deng, W.; Zhao, H.; Pan, F.; Feng, X.; Jung, B.; Abdel-Wahab, A.; Batchelor, B.; Li, Y. Visible-Light-Driven Photocatalytic Degradation of Organic Water Pollutants Promoted by Sulfite Addition. *Environ. Sci. Technol.* **2017**, *51* (22), 13372−13379.
(40) Yuen, Y. T.; Sharratt, P. N.; Jie, B. Carbon Dioxide Mineralization Process Design and Evaluation: Concepts, Case Studies, and Considerations. *Environ. Sci. Poll. Res.* **2016**, *23* (22), 22309−22330.
(41) Jeffery, D. Z.; Camara, G. A. The Formation of Carbon Dioxide during Glycerol Electrooxidation in Alkaline Media: First Spectroscopic Evidences. *Electrochem. Commun.* **2010**, *12* (8), 1129−1132.
(42) Yan, Z.; Liu, W.; Liu, X.; Shen, Z.; Li, X.; Cao, D. Recent Progress in Electrocatalytic Conversion of CO_2 to Valuable C_2 Products. *Adv. Mater. Interfaces* **2023**, *10* (20), 2300186.

https://doi.org/10.1021/acsaem.5c03695
ACS Appl. Energy Mater. 2026, 9, 2197−2208

(43) Yu, J.; Wang, J.; Ma, Y.; Zhou, J.; Wang, Y.; Lu, P.; Yin, J.; Ye, R.; Zhu, Z.; Fan, Z. Recent Progresses in Electrochemical Carbon Dioxide Reduction on Copper-Based Catalysts toward Multicarbon Products. *Adv. Funct. Mater.* **2021**, *31* (37), 2102151.
(44) Saha, P.; Amanullah, S.; Dey, A. Selectivity in Electrochemical CO_2 Reduction. *Acc. Chem. Res.* **2022**, *55* (2), 134−144.
(45) Murthy, A.; Manthiram, A. Application of Derivative Voltammetry in the Analysis of Methanol Oxidation Reaction. *J. Phys. Chem. C* **2012**, *116* (5), 3827−3832.
(46) Caneppele, G. L.; Martins, C. A. Revisiting Glycerol Electrooxidation by Applying Derivative Voltammetry: From Well-Ordered Bulk Pt to Bimetallic Nanoparticles. *J. Electroanal. Chem.* **2020**, *865*, No. 114139.
(47) Yu, Y.; Xie, F.; Chen, R.; Zhu, X.; Liao, Q.; Ye, D.; Li, J.; Song, S. New Insights into the Role of CO2 in a Photocatalytic Fuel Cell. *J. Power Sources* **2021**, *487*, No. 229438.
(48) Zhang, J.; Lv, S.; Zheng, J.; Yang, P.; Li, J.; Wu, X.; Jin, T.; Cheng, C.; Song, Y.; Li, L. Self-CO_2 Recycling Photocatalytic Fuel Cell for Enhancing Degradation of Pollutants and Production of Carbon-Neutral Fuel. *ACS Sustain. Chem. Eng.* **2020**, *8* (30), 11133−11140.
(49) Zhang, J.; Yang, P.; Zheng, J.; Li, J.; Fu, Q.; He, Y.; Zou, Y.; Wu, X.; Cheng, C.; Wang, F. Enhanced Carbon Dioxide Reduction in a Thin-Film Rotating Disk Photocatalytic Fuel Cell Reactor. *J. CO2 Util.* **2020**, *37*, 328−334.
(50) Xie, F.; Chen, R.; Zhu, X.; Liao, Q.; Ye, D.; Zhang, B.; Yu, Y.; Li, J. CO2 Utilization: Direct Power Generation by a Coupled System That Integrates Photocatalytic Reduction of CO2 with Photocatalytic Fuel Cell. *J. CO2 Util.* **2019**, *32*, 31−36.
(51) Jiao, L.; Xie, F.; Chen, R.; Ye, D.; Zhang, B.; An, L.; Yu, Y.; Li, J. Toward CO_2 Utilization for Direct Power Generation Using an Integrated System Consisting of CO_2 Photoreduction with 3D TiO_2 /Ni-Foam and a Photocatalytic Fuel Cell. *J. Mater. Chem. A* **2019**, *7* (11), 6275−6284.
(52) Gomes, L. E.; Plaça, L. F.; Rosa, W. S.; Gonçalves, R. V.; Ullah, S.; Wender, H. Increasing the Photocatalytic Activity of BiVO4 by Naked Co(OH)2 Nanoparticle Cocatalysts. *Photochem* **2022**, *2* (4), 866−879.
(53) Hunge, Y. M.; Uchida, A.; Tominaga, Y.; Fujii, Y.; Yadav, A. A.; Kang, S.-W.; Suzuki, N.; Shitanda, I.; Kondo, T.; Itagaki, M.; Yuasa, M.; Gosavi, S.; Fujishima, A.; Terashima, C. Visible Light-Assisted Photocatalysis Using Spherical-Shaped BiVO4 Photocatalyst. *Catalysts* **2021**, *11* (4), 460.
(54) Sharifi, T.; Crmaric, D.; Kovacic, M.; Popovic, M.; Rokovic, M. K.; Kusic, H.; Jozić, D.; Ambrožić, G.; Kralj, D.; Kontrec, J.; Zener, B.; Stangar, U. L.; Dionysiou, D. D.; Bozic, A. L. Tailored BiVO4 for Enhanced Visible-Light Photocatalytic Performance. *J. Environ. Chem. Eng.* **2021**, *9* (5), No. 106025.
(55) Barreca, D.; Carta, G.; Gasparotto, A.; Rossetto, G.; Tondello, E.; Zanella, P. A Study of Nanophase Tungsten Oxides Thin Films by XPS. *Surf. Sci. Spectra* **2001**, *8* (4), 258−267.
(56) Dan, Z.; Yang, Y.; Qin, F.; Wang, H.; Chang, H. Facile Fabrication of Cu2O Nanobelts in Ethanol on Nanoporous Cu and Their Photodegradation of Methyl Orange. *Materials* **2018**, *11* (3), 446.
(57) Biesinger, M. C. Advanced Analysis of Copper X-ray Photoelectron Spectra. *Surf. Interface Anal.* **2017**, *49* (13), 1325−1334.
(58) Chang, H.-W.; Chen, S.-C.; Chen, P.-W.; Liu, F.-J.; Tsai, Y.-C. Constructing Morphologically Tunable Copper Oxide-Based Nanomaterials on Cu Wire with/without the Deposition of Manganese Oxide as Bifunctional Materials for Glucose Sensing and Supercapacitors. *Int. J. Mol. Sci.* **2022**, *23* (6), 3299.
(59) Gomes, L. E.; Morishita, G. M.; Icassatti, V. E. M.; da Silva, T. F.; Machulek Junior, A.; Rodríguez-Gutiérrez, I.; Souza, F. L.; Martins, C. A.; Wender, H. Enhanced Power Generation Using a Dual-Surface-Modified Hematite Photoanode in a Direct Glyphosate Photo Fuel Cell. *ACS Appl. Mater. Interfaces* **2024**, *16* (14), 17453−17460.

https://doi.org/10.1021/acsaem.5c03695
ACS Appl. Energy Mater. 2026, 9, 2197−2208